Supplementary Information for

Full title: Graphene enhanced Brillouin optomechanical microresonator for ultra-sensitive gas detection

Baicheng Yao,[*,†,‡,§] *Caibin Yu,*[†] *Yu Wu,*[†] *Shu-Wei Huang,*[‡] *Han Wu,*[†] *Yuan Gong*[†,∥]

Yuanfu Chen,[⊥] *Yanrong Li,*[⊥] *Chee Wei Wong,*[‡] *Xudong Fan,*[∥] *Yunjiang Rao*[*,†]

[†]Key Laboratory of Optical Fiber Sensing and Communications (Education Ministry of China), University of Electronic Science and Technology of China, Chengdu 610054, China.
[‡] Fang Lu Mesoscopic Optics and Quantum Electronics Laboratory, University of California, Los Angeles, CA 90095, United States.
[§]Cambridge graphene center, University of Cambridge, CB3 0FA, United Kingdom.
[∥]Department of Biomedical Engineering, University of Michigan, Ann Arbor, MI 48109, United States.
[⊥]State Key Laboratory of Electronic Thin Films and Integrated Devices, University of Electronic Science and Technology of China, Chengdu 610054, China.

Email: by252@cam.ac.uk; yjrao@uestc.edu.cn

The supplementary materials consist of:

S1. Theoretical analysis

S1.1. Forward stimulated Brillouin scattering in WGM cavities

In the WGM cavity supporting both surface acoustic modes and high density optical modes, phase matching condition of the forward stimulated Brillouin scattering (F-SBS) could be satisfied in different modes [S1], Stokes line could be generated from the pump, obeying:

$$f_p = f_s + f_M \tag{S1}$$

$$\vec{k}_p = \vec{k}_s + \vec{k}_M \tag{S2}$$

In the cavity, the generated acoustic surface modes and the optical modes have the same propagation direction approximately. Referring to the optical dispersion and the acoustic dispersion, Eq. (S2) could be transferred as

$$\frac{f_M}{v_A} = \frac{2\pi f_p n_p}{c} - \frac{2\pi f_s n_s}{c} \tag{S3}$$

Here v_A is the acoustic velocity, $c = 3\times10^8$ m/s is the light velocity in vacuum, n_p and n_s is the effective index of the pump mode and the generated Stokes mode. Considering Eq. (S1), we can get the relationship of the f_p and the f_s:

$$f_s = \frac{c - 2\pi v_A n_p}{c - 2\pi v_A n_s} f_p \tag{S4}$$

For a WGM resonator, it can support several transverse modes, which has varied effective indexes and FSRs -- any of them can be marked as $TM_{XY,N}$. Here subscript *X*, *Y*, *and Z* shows the order of the transverse modes (determined by the geometry) and the longitude mode (determined by the optical frequency), respectively. By using finite element method and commercial software COMSOL MULTIPHYSICS 4.3, Figure S1a to 1c simulate 3 examples of the WGM modes in our silica bottle-shaped cavity (diameter 118 μm and wall thickness 8 μm, index of the silica 1.454 at 1550 nm). In the resonator, to accumulate enough energy higher than the nonlinear threshold and the detection threshold, both the pump and the generated Stokes line of the F-SBS should be located at high *Q* resonant frequencies, and the transverse modes of them are different. Transverse mode order of f_s is higher than that of f_p.

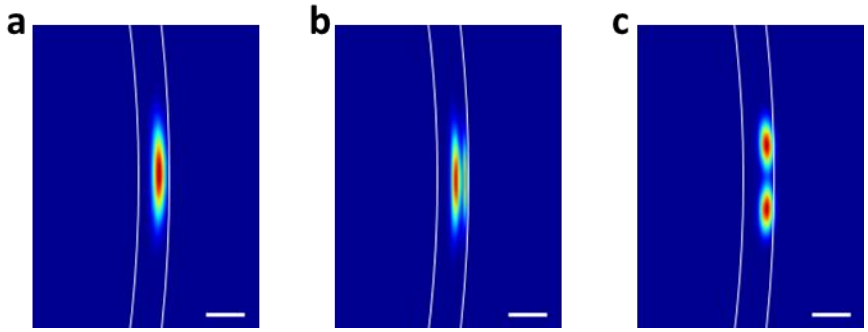

Fig. S1. Simulated electric field distributions (sectional view). a, $TM_{01,347}$, (λ = 1551.9 nm), **b,** $TM_{11,342}$, (λ = 1561.0 nm), **c,** $TM_{02,346}$, (λ = 1544.2 nm). In this figure the bar shows 10 μm.

Commonly, intensity of the phonon excitation is proportional to the pump power P_p, and the effective transmission length L_{eff}, as

$$I_M \propto \exp\left[g_B P_p L_{eff} / A_{eff} \right] \quad \text{(S5)}$$

Here g_B is the Brillouin gain coefficient, A_{eff} is the effective transverse mode field distribution. In the resonator, L_{eff} is determined by the Q factor, i.e. a higher Q brings a larger L_{eff}. For instance, in our GBMR with $Q \approx 2\times10^6$, L_{eff} of the TM_{01} mode could be as long as tens of kilometers, which is helpful reducing F-SBS threshold lower than 1 mW.

S1.2. Reduced graphene oxide film enhances the F-SBS

Graphene enhances the F-SBS via influencing the g_B and the L_{eff} of the pump mode majorly. Here L_{eff} relates to the loss while g_B is determined by the material,

$$g_B \propto \frac{4\pi^2 \gamma_e^{\,2}}{n_p c \lambda_p^{\,2} \rho_0 v_A \Gamma_B} \quad \text{(S6)}$$

Here γ_e is the electrostrictive coefficient, n_p is the effective index of the pump mode, Γ_B is the lifespan of the phonons. Determined by its permittivity, the rGO film has high optical index: n_{rGO} is higher than 3 in *C*-band [S2,S3]. As a result, at the same frequency, n_p of a specific pump mode in the graphene based WGM cavity is smaller than the one in the silica cavity, and high order modes are enhanced, hence L_{eff} of high order modes increase. Moreover, rGO brings a much higher γ_e than silica [S4], consequently, g_B could be enhanced in the rGO based WGM cavity.

S1.3. Gas adsorption based phonon excitation

In the GBMR, gas detection relies on the phase matching of the optomechanical modes. Spectral shift of the f_s is determined by the v_A majorly:

$$\frac{\partial f_s}{\partial x} = \frac{2\pi n_s - 2\pi n_p}{\left(c - 2\pi v_A n_s\right)^2} \frac{\partial v_A}{\partial x} f_p \tag{S7}$$

Here x is the gas concentration, $n_s < n_p$, and we approximately assume the change of the n_s is negligible. This equation reveals that when v_A decreases with gas concentration, f_s increases accordingly, which also verifies that $f_M = f_p - f_s$ decreases when launching a higher gas concentration. In terms of the v_A, it obeys the media equation $v_A = (E_Y/\rho)^{1/2}$, wherein E_Y is the elastic modulus of the cavity, and ρ is the density. According to previous researches, gas adsorption induced surface defect in the rGO film reduces the E_Y. Figure S2 plots the theoretically calculated results. With gas concentration increasing, graphene's elastic modulus decreases from ≈ 1.15 TPa to 1.09 TPa, while the effective acoustic velocity of the graphene-silica cavity decreases from ≈ 5660 m/s to 5480 m/s. In our GBMR, the effective inner surface area deposited by rGO is 2.6×10^{-2} mm^2, the number of NH_3 gas molecules adsorbed on the is on 10^{11} level.

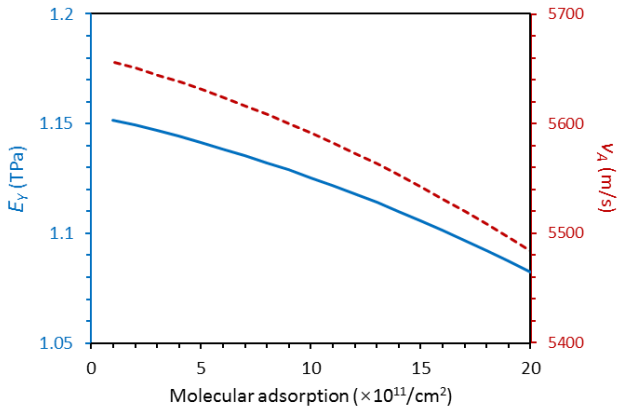

Fig. S2. Calculated results of the elastic modulus of the rGO (blue solid curve), and the acoustic velocity of the cavity (red dashed curve).

S2. Fabrication of the graphene enhanced Brillouin microresonator (GBMR)

Fabrication process of the GBMR for WGM resonance is shown in Figure S3a. First, commercial silica capillary (CV17-100) with 100 μm outer diameter and 17 μm thick wall

was fixed in a programmable fiber splicer (Fusion FITEL-S184, JPN). By setting parameter '150 mA/200 ms + 200mA / 100 ms', we heated the capillary via arc discharge. Due to thermal expansion of the internal air, fused silica capillary was reformed to be a Bottle cavity. The fabricated Bottle cavity has a diameter of 118 μm and a minimum wall thickness of 8 μm. Then it was washed by alcohol and DI water.

1 mg Graphene oxide powder was dissolved in 100mL DI water with sonication for 2 hours to form a uniform dispersion. Then the GO dispersion was injected into the capillary via fluidic tube. After 24 hours, the water of the GO dispersion was evaporated naturally in air at room temperature, therefore the thin GO film was deposited on the inner wall of the Bottle cavity. Afterwards we injected hot Vitamin C aqueous solution (20g/L) in the capillary, keeping the GO film reduced by the Vitamin C solution (40 ^{o}C) for 1.5 hour. Then the GO film was reduced to be a thin rGO film. Finally, the rGO based capillary was washed by DI water for several times and gently dried on a heat-port. We also described this technique in Ref. (29). It is worth noting that to ensure the rGO film uniform and thin (to avoid too much loss), solution concentration should be low and the reduction process should be controlled slow. Figure S3b and S3c shows the X-ray photoelectron spectra (XPS) of the GO film and the rGO film, respectively. Compared to the GO film, the rGO film has $\approx$ 2 times higher C:O ratio, implying that the reduction is effective.

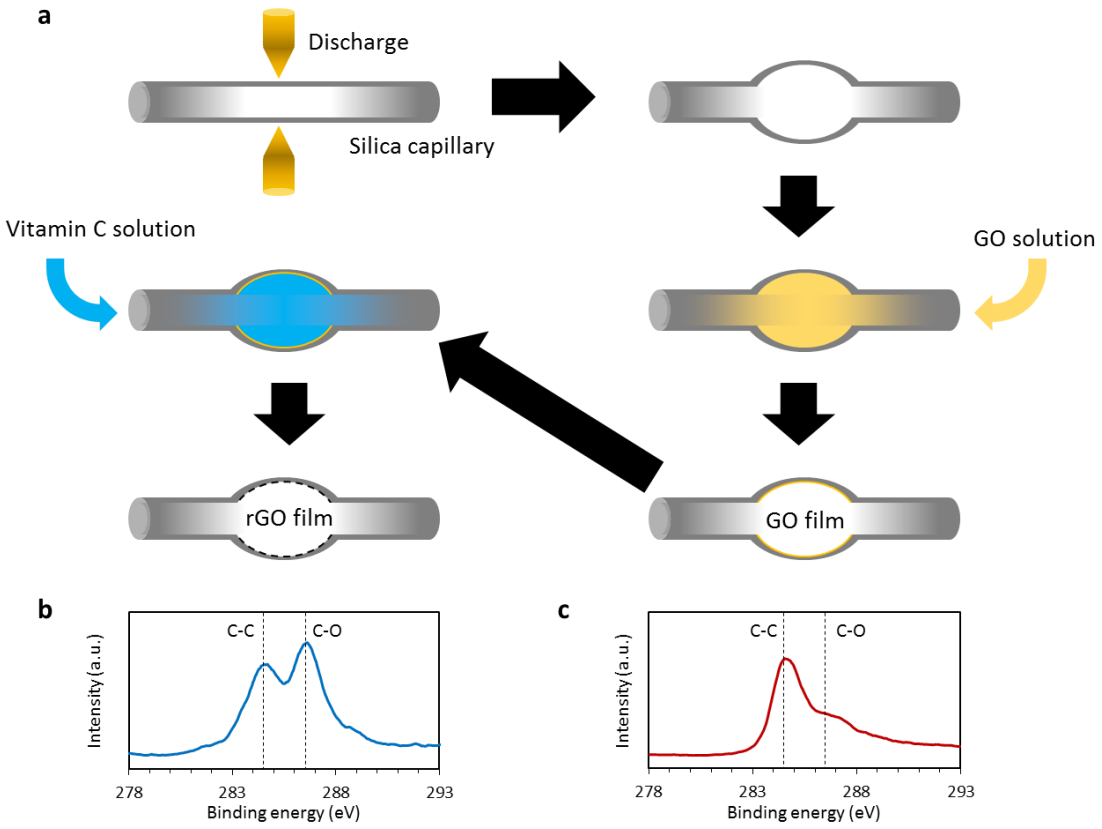

Fig. S3. Fabrication of the GBMR. a, The silica bottle cavity was bubbled by a fiber splicer, and then rGO film was deposited in its inner wall via Vitamin C reduction. **b,** XPS of the GO film, **c,** XPS of the rGO film.

S3. Measuring optical *Q* factors of the WGM resonators

Figure S4c plots the measured *Q* factors of the 3 types for fundamental mode resonances around 1550 nm: Determined by the dimensional restrictions, the cylindrical capillary has a typical *Q* factor is $\approx 10^6$; the bottle-shaped capillary can have a much higher *Q* factor approaching 8×10^6; and the microsphere has the highest *Q* factor > 1.4×10^7. However, gas flow cannot pass through the microsphere. Hence, the bottle-shaped capillary with both a through channel for gas flow and a relatively high *Q* factor is adopted in this work. Figure S4d provide two more resonance dip examples of the bottle-shaped cavity, with central wavelength at 1534.7 nm (fundamental mode, Q $\approx 8\times10^6$) and 1592.3 nm (fundamental mode, Q $\approx 7\times10^6$). Figure S4e provide two more resonance dip examples of the GBMR

cavity, with central wavelength at 1534.6 nm (fundamental mode, Q ≈ 2×10^6) and 1594.1 nm (fundamental mode, Q ≈ 1.8×10^6). For wavelength in range of 1530 nm to 1570 nm, the *Q* factor of the fundamental mode in the bottle-shaped cavity keeps ≈ 8×10^6, and the *Q* factor of the fundamental mode in the GBMR cavity keeps ≈ 2×10^6. For lower optical frequencies (> 1580 nm), due to scattering based loss, the *Q* factor would be a bit lower.

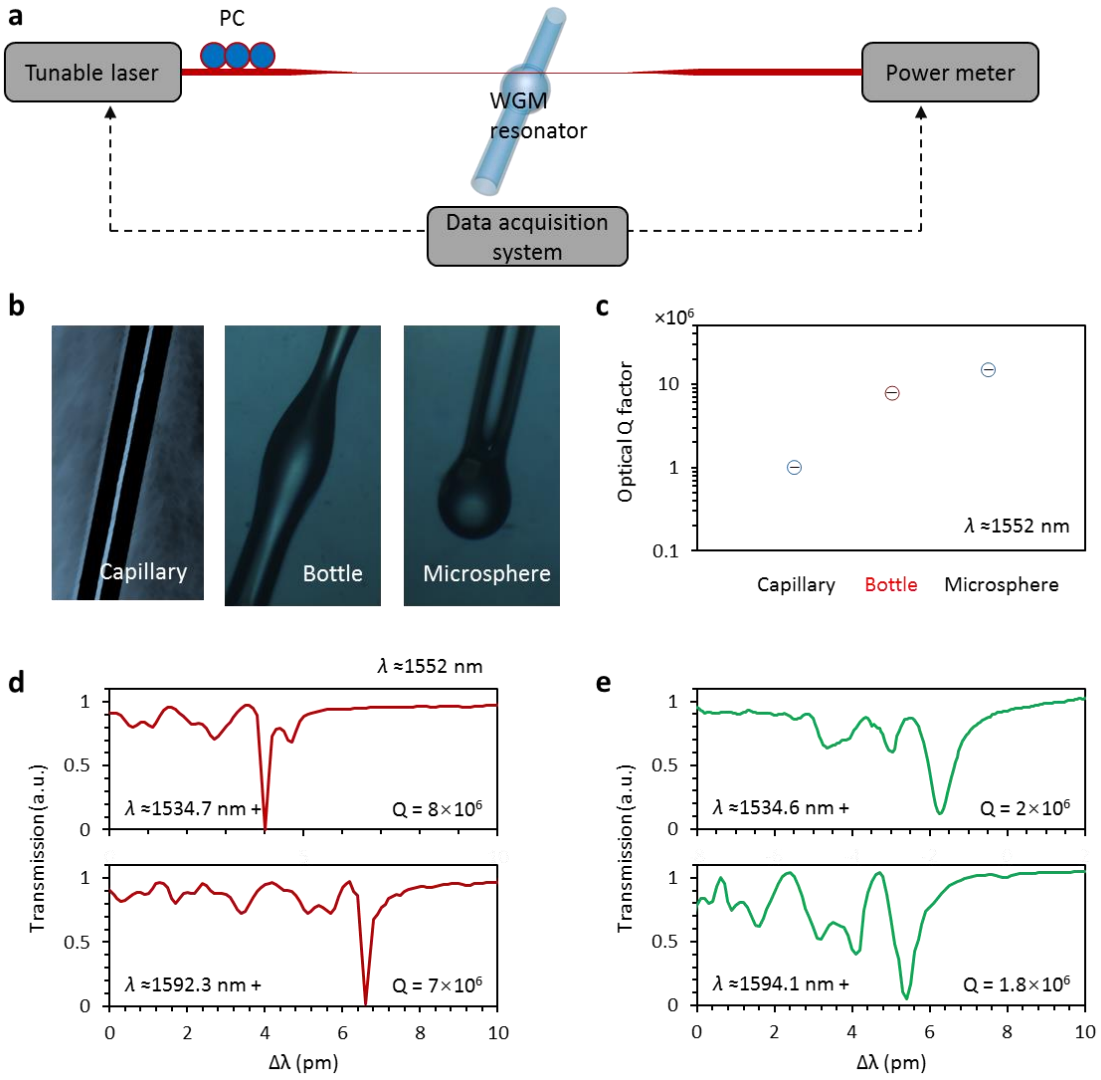

Fig. S4. Measurement of the transmissions and optical *Q* factors. a, Experimental setup. **b,** Three different WGM resonators. **c,** Optical *Q* factor of the resonators for fundamental mode at wavelength ≈ 1552 nm. **d,** Two examples of resonance dips of the bottle-shaped WGM microresonator. **e,** Two examples of resonance dips of the GBMR.

S4. Experimental setup and preparation of the gas samples

Figure S5 shows the experimental setup to generate the F-SBS and detect the gas concentration. A tunable laser (Agilent B1636B, USA, resolution 1 pm) works as the pump, which is carefully tuned in the resonances to find the F-SBS. A fiber polarization controller (FPC) is used to control the coupling modes. Collected light from the WGM cavity is launched in a photodetector (Thorlabs, USA, 1.25GHz) and a high resolution OSA (APEX AP2051A, France, resolution 0.02 pm), via an optical fiber coupler. The beat note is monitored by a RF spectroscope (Agilent N9020A, USA). In experiment, we carefully tune the pump frequency to find phase-matched point, in span of 1520 nm to 1590 nm, by monitoring the beat note on RF spectroscope. Considering the generated F-SBS intensity, SNR, frequency, and stability together, we select the mechanical mode in order of 24 (f_M = 262 MHz) for gas detection. In gas detection, the pump frequency and polarization is fixed.

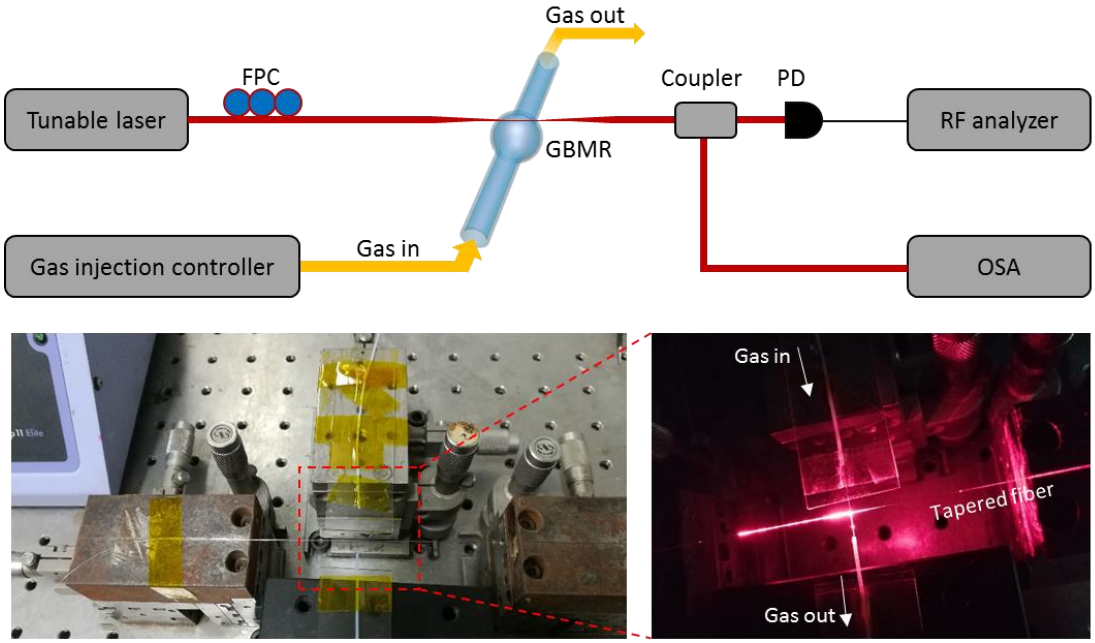

Fig. S5. Experimental setup. Red path: optical fibers, black path: electronics, Yellow arrows: gas direction. FPC: fiber polarization controller, PD: photodetector.

Figure S6 shows the process we prepare NH_3 gas samples with concentration of 1 ppm to 20 ppm. First, pure NH_3 gas (100% concentration) is drawn out from the gas chamber, by using micro syringe. The volume is controlled as 1 μL, 2 μL, 3 μL, 4 μL, 5 μL, 10 μL, and 20 μL, respectively. Then the pure NH_3 gas is injected another gas buffer, whose

volume is 1 L. Hence we get NH_3 samples with concentration of 1 ppm to 20 ppm. Finally the samples with certain concentration is injected into the GBMR.

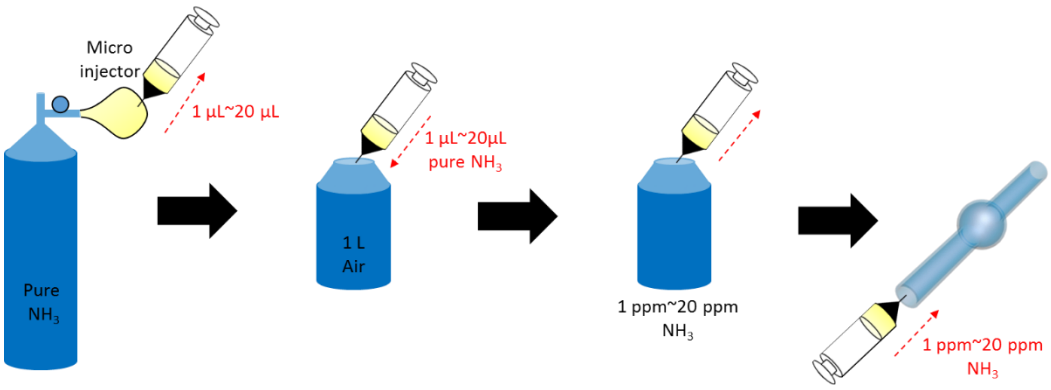

Fig. S6. Preparing the gas samples. By using micro syringe, pure NH_3 gas is diluted to be 1 ppm ~ 20 ppm and then launched into the GBMR.

S5. Gas detection experiment based on BMR without rGO film deposition

BMR without graphene material can support resonant multimodes and F-SBS generation as well. Figure S7 maps the spectrum of a mechanical mode (We select a mode with similar order to the one in the GBMR) generated in a BMR, varying with NH_3 gas concentration change. Because there is no material to adsorbing the gas molecules, the beat note cannot shift obviously, obeying the fixed phase-matching condition. Related to previously reported μFOM structure measuring liquid [S5], NH_3 gas cannot affect the silica cavity so much.

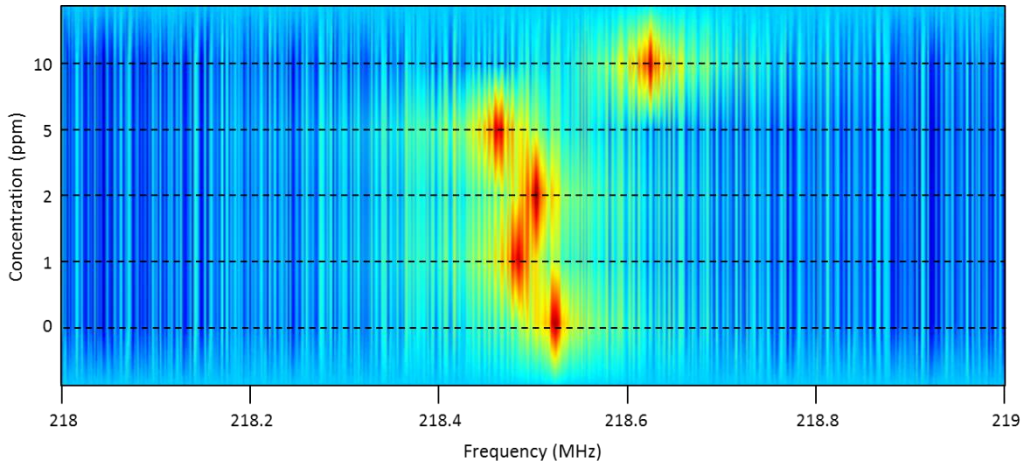

Fig. S7. Spectral response of the BMR. By increasing the NH_3 gas concentration, there is no obvious change on the spectra.

S6. Instability of the GBMR

Figure S8a and S8b show the measured power instability and the spectral uncertainty of the mechanical resonance (Mode 24 at 262 MHz) during gas detection, respectively. At each gas concentration, we sample 10 points (1 point per second). As Figure S8a plots, amplitude instability of the GBMR is ≈8 dB, which is influenced by the thermal noise, the Brillouin gain, the detuning, and the PD accuracy, etc. Fortunately, SNR of the beat note keeps > 30 dB, the spectral location of the beat note could still be extract in high resolution. Corresponding to the main text, Figure S8b plots the uncertainty of the beat note spectrally. It varies in hundreds Hz. A higher gas concentration tends to bring stronger instability.

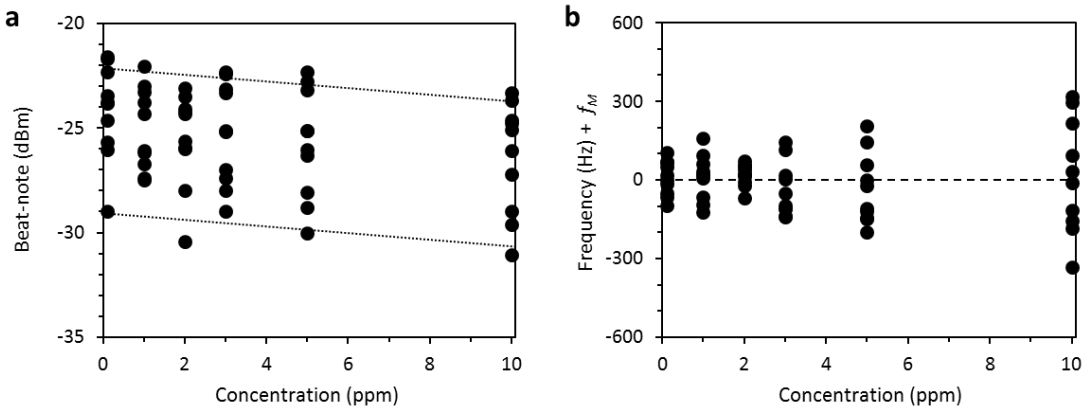

Fig. S8. Uncertainty of the resonant mode in the GBMR. a, power instability. **b,** Spectral instability. In **a**, the dashed lines show the average edge of the power instability, in **b**, the dashed line shows the central frequency.

S7. Supplementary discussion about the performances

Table S1 concludes the comparison of the performances of recent gas sensors. Related of the state-of-literature optical gas sensors, this work shows unique advantages. *NG means *Not Given*.

Table. Comparison of state-of-art optical gas sensors

Sensor type	Detect limit	Dynamic range	Response speed	Compactness	Reference
Photothermal spectroscopy	2 ppb	6 orders	minutes	meters long	S6
Graphene based optical interferences	sub ppm	2 orders in average	seconds	cm level	S7
Graphene based SPR	1 ppm	NG	minutes	NG	S8
Ultrasensitive plasmonic sensors	~ ppm	NG	NG	tens of cm	S9
Visible spectroscopy	5 ppb	NG	minutes	NG	S10
Graphene enhanced SBS	**1 ppb**	**5 orders**	**seconds**	**<cm**	**This work***

Supplementary References

S1 Matsko, A., Savchenkov, A., Ilchenko, V., Seidel, D. & Maleki, L. Optomechanics with surface-acoustic-wave whispering-gallery modes. Phys. Rev. Lett. 103, 257403 (2009).

S2. Vakil, A. & Engheta, N. Transformation optics using graphene, Science 332, 1291 (2011).

S3. Yao, B. Wu, Y., Wang, Z., Cheng, Y., Rao, Y., Gong, Y., Chen, Y. & Li, Y. Demonstration of complex refractive index of graphene waveguide by microfiber-based Mach–Zehnder interferometer. Opt. Express 21, 29818-29826 (2013).

S4. Rodrigues, G., Zelenovskiy, P., Romanyuk, K., Luchkin, S., Kopelevich, Y. & Kholkin, A. Strong piezoelectricity in single-layer graphene deposited on SiO2 grating substrates. Nature Comm. 6, 7572 (2015).

S5. Kim, K. & Fan, X. Surface sensitive microfluidic optomechanical ring resonator sensors. Appl. Phys. Lett. 105, 191101 (2014).

S6. Jin, W., Cao, Y., Yang, F. & Ho, H. Ultra-sensitive all-fiber photothermal spectroscopy with large dynamic range. Nat. Comm. 6, 7767-7775 (2015).

S7. Shivananju, B., Yu, W., Liu, Y., Zhang, Y., Lin, B., Li, S. & Bao, Q. The roadmap of graphene-based optical biochemical sensors. Adv. Funct. Mat. (2017): DOI: 10.1002/adfm.201603918.

S8. Cittadini, M., Bersani, M., Perrozzi, F., Ottaviano, L., Wlodarski, W., Martucci, A. Graphene oxide coupled with gold nanoparticles for localized surface plasmon resonance based gas sensor. Carbon 69, 452–459 (2014).

S9. Caucheteur, C., Guo, T., Liu, F., Guan, B., Albertc, J. Ultrasensitive plasmonic sensing in air using optical fibre spectral combs. Nature Comm. 7, 13371 (2016).

S10. Lehner, P., Staudinger, C., Borisov, S., Klimant, I. Ultra-sensitive optical oxygen sensors for characterization of nearly anoxic systems. Nature Comm. 5, 4460 (2014).